

Validation of the quasi-steady performance model for pumping airborne wind energy systems

Schelbergen, Mark; Schmehl, Roland

DOI

[10.1088/1742-6596/1618/3/032003](https://doi.org/10.1088/1742-6596/1618/3/032003)

Publication date

2020

Document Version

Final published version

Published in

Journal of Physics: Conference Series

Citation (APA)

Schelbergen, M., & Schmehl, R. (2020). Validation of the quasi-steady performance model for pumping airborne wind energy systems. *Journal of Physics: Conference Series*, 1618(3), Article 032003. <https://doi.org/10.1088/1742-6596/1618/3/032003>

Important note

To cite this publication, please use the final published version (if applicable). Please check the document version above.

Copyright

Other than for strictly personal use, it is not permitted to download, forward or distribute the text or part of it, without the consent of the author(s) and/or copyright holder(s), unless the work is under an open content license such as Creative Commons.

Takedown policy

Please contact us and provide details if you believe this document breaches copyrights. We will remove access to the work immediately and investigate your claim.

PAPER • OPEN ACCESS

Validation of the quasi-steady performance model for pumping airborne wind energy systems

To cite this article: Mark Schelbergen and Roland Schmehl 2020 *J. Phys.: Conf. Ser.* **1618** 032003

View the [article online](#) for updates and enhancements.



IOP | ebooks™

Bringing together innovative digital publishing with leading authors from the global scientific community.

Start exploring the collection—download the first chapter of every title for free.

Validation of the quasi-steady performance model for pumping airborne wind energy systems

Mark Schelbergen and Roland Schmehl

Faculty of Aerospace Engineering, Delft University of Technology, Kluyverweg 1, 2629 HS Delft, The Netherlands

E-mail: m.schelbergen@tudelft.nl

Abstract. The quasi-steady performance model (QSM) has been developed specifically for pumping airborne wind energy systems using flexible membrane wings. In this study, we validate this model using a comprehensive set of flight data that includes 87 consecutive pumping cycles and is acquired with the development platform of Kitepower B.V. The aerodynamic properties of the kite are determined using onboard measurements of the relative flow velocity. We found that neglecting the vertical wind component and straightening and slacking motion of the tether lead to substantial errors in the kite velocity calculated using the system model. A reasonable agreement between the QSM simulations and flight data can be obtained by multiplying the kite's drag coefficient by a fudge factor and thereby turning the QSM into a grey-box model. The model accuracy is statistically evaluated as opposed to only evaluating a single pumping cycle per system configuration as done in earlier research.

1. Introduction

Airborne wind energy (AWE) is a relatively new technology. Currently, no commercial systems are in operation yet. Consequently, little operational data is available for scientific purposes. A key performance indicator of a wind energy system is its annual energy production (AEP). Calculating the AEP requires a wind resource representation, a performance model, and adequate coupling of the two.

Schelbergen [8] developed a wind resource representation for AEP calculations specifically for AWE in which the wind resource is characterised using a set of wind profile shapes identified using a data-driven approach. Alternatively, Malz [4] uses a brute force approach by directly using the full three-hourly dataset of one year to calculate the AEP.

The quasi-steady performance models (QSM) proposed by Van der Vlugt [10] and Ranneberg [7] move the kite along a prescribed flight path. The former is used in performance optimisations by Schelbergen [8]. To assess the validity of the QSM, Van der Vlugt roughly compares the simulation results to the flight data of two pumping cycles flown on different days in moderate and strong winds, with different kites, and without air flow measurements at the kite.

Numerous dynamic models have been developed with varying complexity. The six degrees of freedom, dynamic model proposed by Gros [3] is very suitable for (performance) optimisation due to its formulation in Cartesian coordinates. Malz [5] uses the latter model in an optimal control problem to fit a simulated flight path to flight measurements of the rigid-wing AP2 prototype of Ampyx Power and finds an error of the predicted mechanical mean cycle power of



Content from this work may be used under the terms of the [Creative Commons Attribution 3.0 licence](https://creativecommons.org/licenses/by/3.0/). Any further distribution of this work must maintain attribution to the author(s) and the title of the work, journal citation and DOI.

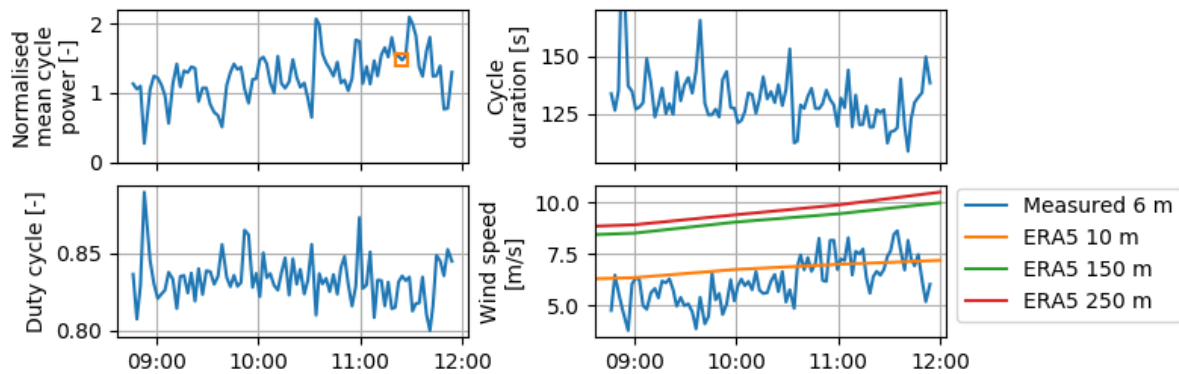


Figure 1. Evolution of the key performance indicators and the mean cycle wind speed from anemometer measurements at the ground station over the 87 pumping cycles. The latter plot is complemented with ERA5 (reanalysis) wind speeds at three heights. The reference pumping cycle is indicated with \square in the upper-left panel.

only 1.2%. The study shows that the straight tether assumption is appropriate for estimating the power production of the analysed flight. The optimal control problem formulation of Malz served as a starting point for developing the Awebox [2]: a toolbox for modelling and optimal control of multiple kite AWE systems.

The degree to which the AWE performance models are validated is generally limited. No validation studies are published that cover a wide spectrum of wind conditions and assess the accuracy of AEP estimations.

This paper starts with discussing the flight data and introducing the reference pumping cycle in Sect. 2. Section 3 discusses how the apparent wind velocity and wind conditions at the kite are reconstructed. In Sect. 4, the aerodynamic coefficients of the kite are identified using a steady kite model. Together with the reconstructed wind speeds, these are used as input to assess the validity of a steady system model. In Sect. 5, simulations are performed using a QSM and the validity of the model is evaluated for all 87 pumping cycles in the dataset. Finally, Sect. 6 summarises the conclusions.

2. Flight test data

The flight test data was recorded on 8 October 2019 at the former naval air base Valkenburg in the Netherlands. For this specific experiment, the 100 kW ground station was equipped with the 25 m² leading edge inflatable V3 kite, which was also used in 2017 by Oehler [6]. The V3 kite has originally been designed for the 20 kW demonstrator system of Delft University of Technology and was first used in 2012. Conservative operational settings were used as the test was focused on data acquisition rather than maximising energy production.

In approximately three hours the system completed 87 pumping cycles in moderate wind conditions. The duty cycle is defined as the ratio of the reel-out and cycle duration. As the wind speed increased with time, the cycle duration and duty cycle decreased, as can be seen in Fig. 1. The 73th pumping cycle is selected as reference cycle because it does not show any anomalies in the wind conditions to which it is exposed and its operation and performance. Figure 2 shows the trajectory flown by the kite in this cycle. All the given power ratings in this paper are normalised with a reference value, which we have chosen to be 1.31 kW (explained in Sect. 5). The power produced in this flight test do not represent the state of the art of Kitepower's system, which normally employs a much larger kite and different operational settings.

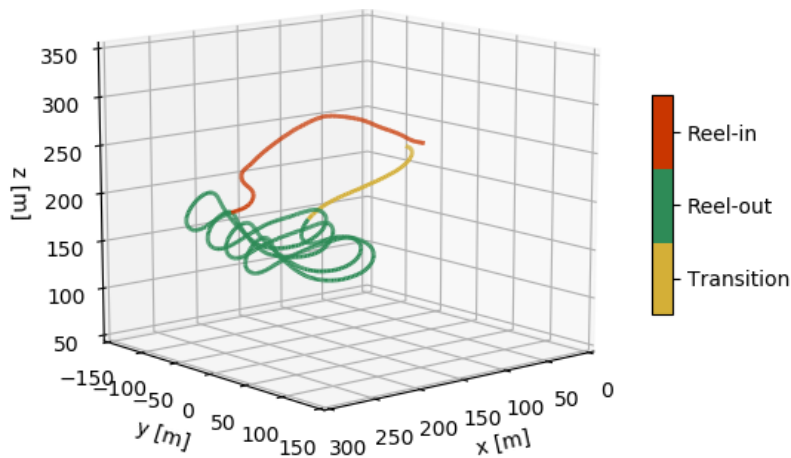


Figure 2. Flight trajectory of the kite of the reference pumping cycle. The trajectory segments of the three cycle phases analysed in Sect. 5 are plotted using different colors.

For this specific flight test, the kite was equipped with a Pixhawk[®], which includes an IMU and GPS sensor for recording the position and attitude of the kite. The Pixhawk[®] was mounted to the strut closest to the symmetry plane of the kite, as shown in Fig. 3, and its default Kalman filter implementation is used for enhancing the position and attitude signals. The air speed was measured using a rigidly-mounted Pitot tube together with a wind vane measuring the air flow direction in the kite's symmetry plane. The flow sensors are mounted to the front bridle lines at one of the node points. The side slip angle is not measured. Moreover, the tether force and the reel-out speed were measured at the ground station. The measured signals for the reference cycle are plotted (labelled with subscript m) in the left panels of Fig. 4.

3. Obtaining wind properties

The measurements enable reconstructing the wind properties at the varying height of the kite. First, the apparent wind velocity is determined based on the flow measurements. The wind velocity at the kite results from subtracting the kite velocity from the apparent wind velocity. The obtained wind properties are used as input for the models that are analysed in the next section.

3.1. Reconstructing the apparent wind velocity

The Pitot tube measurements are assumed to be insensitive to misalignment with the inflowing air. The apparent wind velocity \mathbf{v}_a expressed in the measurement reference frame, denoted by superscript m , is reconstructed from the air flow measurements:

$$\mathbf{v}_a^m = v_m \begin{bmatrix} -\cos \alpha_m \\ 0 \\ \sin \alpha_m \end{bmatrix}, \quad (1)$$

in which v_m is the air speed measured by the Pitot tube, which is aligned with the x_m -axis, and α_m is the inflow angle measured by the wind vane. The side slip angle and thus the lateral apparent wind velocity component are assumed to be zero. This assumption implies that the kite is always heading into the apparent wind. In the experiment of Oehler [6], recordings of side slip angles up to ten degrees were common, which should be taken in mind when interpreting the results of this study. For future flight tests, a second wind vane will be added to the measurement setup for measuring the side slip angle.

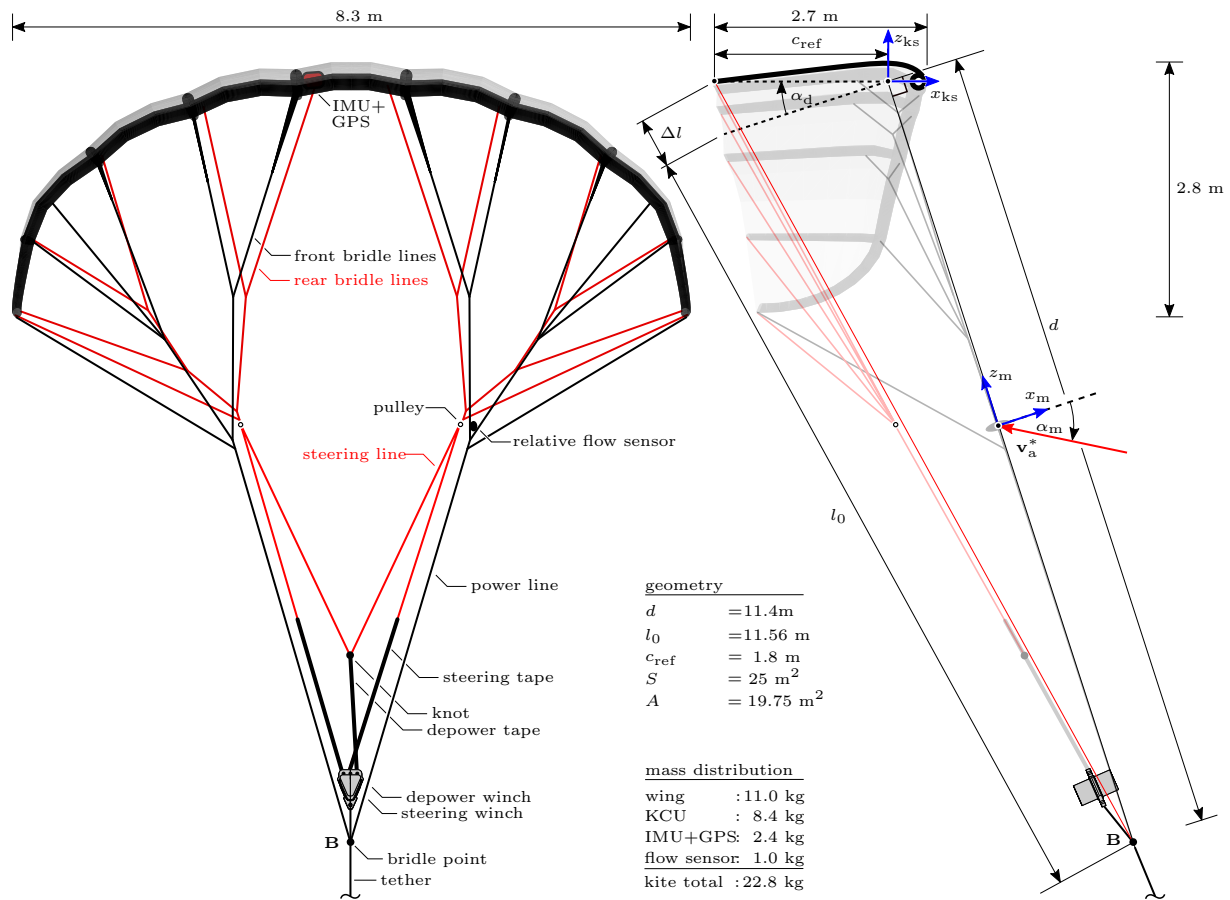


Figure 3. Front-view (left) and side-view (right) of the V3 kite adapted from [6]. The side-view shows the revised flow measurement and kite sensor reference frames.

The measurements yield the flow properties expressed in the measurement reference frame. We would like to have the flow properties expressed in the kite sensor reference frame, since also the orientation of the kite is expressed in this reference frame. The transformation from the measurement to the kite sensor reference frame is done by a single pitch down rotation with the angle α_d . This angle varies depending on the power setting of the kite. A simple geometrical model is used to approximate the pitch down angle as a function of the power setting based on the cosine rule:

$$\cos(\alpha_d + 90^\circ) = \frac{d^2 + c_{ref}^2 - (l_0 + \Delta l)^2}{2 d c_{ref}}, \quad (2)$$

where $d = 11.4$ m is the length along the power lines between the bridle point and the chord in the x_m, z_m -plane, $c_{ref} = 1.8$ m is the length along the chord line between the front and rear bridle line connections, l_0 is the length along the de-power tape between the bridle point and the chord in the x_m, z_m -plane, for which $\alpha_d = 0^\circ$ and the power setting $u_{p,ref} = 0.82$, and Δl is the difference in this length due to a power setting u_p other than the reference value and is given by:

$$\Delta l = \frac{\Delta l_d}{2} = -\frac{u_p - u_{p,ref}}{2} l_d, \quad (3)$$

in which $l_d = 5$ m is the de-power tape length difference between the fully powered and de-

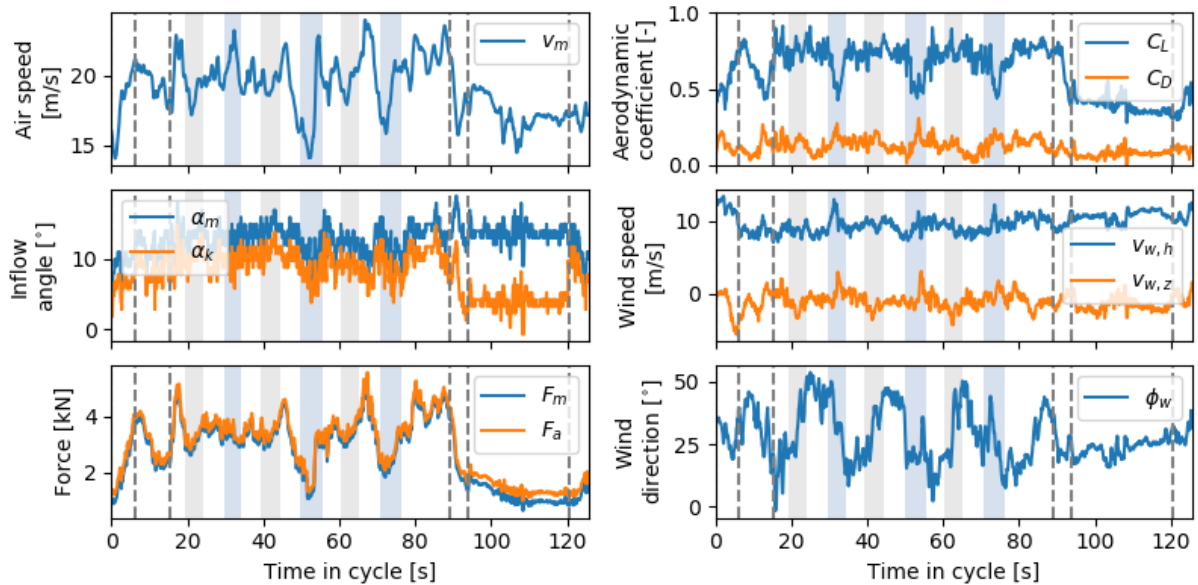


Figure 4. Measured flow, measured tether force, and calculated properties during the reference pumping cycle. The reel-out and reel-in phase take place between 15–89s and 94–121s, respectively. The grey and blue shade indicate right and left turns, respectively.

powered setting: $u_p = 1$ and $u_p = 0$, respectively. Note that Δl is half the de-power tape length difference due to the pulley connection between the de-power tape and the rear bridles. The angle of attack experienced by the kite α_k in the symmetry plane is:

$$\alpha_k = \alpha_m - \alpha_d \quad . \quad (4)$$

From the left, upper two panels of Fig. 4 we can observe that the measured air speed and inflow angle drop substantially during the second and third left turns and not during right turns. Possible causes for these drops are the asymmetry of the flow measurement setup and a misalignment of the crosswind patterns and the wind direction due to wind veer. The power settings during the reel-out and reel-in phases are 0.78 and 0.7, respectively. In line with the conservative operational approach, the difference in power setting between the phases is small.

3.2. Reconstructing the wind conditions

When assuming that the kite does not induce a velocity variation to the free stream wind velocity, the wind velocity \mathbf{v}_w at the kite can be determined from the apparent wind \mathbf{v}_a and kite velocity \mathbf{v}_k :

$$\mathbf{v}_w = \mathbf{v}_a + \mathbf{v}_k \quad . \quad (5)$$

By expressing the wind velocity in the earth reference frame, the horizontal wind speed $v_{w,h}$ and downwind direction ϕ_w can be determined. From the middle-right panel of Fig. 4, we can observe that the horizontal wind speed is reasonably constant and that, as expected, the vertical wind speed is close to zero. The lower-right panel of Fig. 4 shows a cyclic pattern in the wind direction synchronous to the figure-of-eight cross-wind manoeuvres: between the right and left turns we observe larger angles than between the left and right turns. This indicates a flaw in the calculation, which is possibly caused by the zero side slip assumption or the misalignment of the kite and measurement setup due to steering.

Figure 5 shows an increasing trend of the wind speed with height due to wind shear. For the reference pumping cycle, the fitted neutral logarithmic profile agrees reasonably well with the wind profile that is obtained from ERA5 reanalysis data [1]. Not shown here is that for some other cycles substantial differences are observed between the reconstructed wind speeds and ERA5. Also the spread around the logarithmic profile is moderate for the reference pumping cycle relative to other cycles.

4. Steady state analyses

First, a steady kite model is used for identifying the lift and drag coefficient of the kite. Subsequently, the identified coefficients and the previously reconstructed wind speeds are used as input for a steady system model to approximate the instantaneous kite velocity. The modelled and measured kite velocities are compared. Note that we only evaluate the instantaneous states and not how they evolve over time.

4.1. Identifying the lift and drag coefficients

The identification of the lift and drag coefficients assumes a steady state of the kite and is similar to the identification performed by Oehler [6]. The main differences are in the flow measurement setup and in deriving the kite attitude. We use a rigidly-mounted instead of a self-aligning Pitot tube. Moreover, we use the measured attitude instead of employing an iterative procedure for finding the attitude that yields a force equilibrium.

The aerodynamic kite force \mathbf{F}_a is determined from the equilibrium of forces acting on the kite:

$$\mathbf{F}_a = -(\mathbf{F}_{g,k} + \mathbf{F}_{g,t} + \mathbf{F}_{D,t} + \mathbf{F}_t^*) \quad , \quad (6)$$

in which $\mathbf{F}_{g,k}$ is the weight of the kite and $\mathbf{F}_{g,t}$, $\mathbf{F}_{D,t}$, and \mathbf{F}_t^* are forces lumped to the kite that follow from the tether weight, drag, and traction force, respectively. The definitions of these forces are adopted from the work of Van der Vlugt [10]. Only the lumped tether drag is defined differently. We assume it to be aligned with the measured instead of the modelled apparent wind velocity. The approximated aerodynamic force and the tether force measured at the ground F_m have roughly the same magnitude, as shown in the lower panel of Fig. 4. This implies that the aerodynamic force is mostly counterbalancing the tether traction force.

The aerodynamic coefficients are obtained by solving the lower system of equations:

$$\begin{bmatrix} F_{a,x}^k \\ F_{a,z}^k \end{bmatrix} = \frac{1}{2} \rho v_{a,xz}^k{}^2 A \begin{bmatrix} \mathbf{e}_\perp^k & \mathbf{e}_\parallel^k \end{bmatrix} \begin{bmatrix} C_L \\ C_D \end{bmatrix} \quad , \quad (7)$$

in which properties expressed in the kite sensor reference frame are denoted by superscript k, $F_{a,x}^k$ and $F_{a,z}^k$ are the aerodynamic force components, ρ is the air density, $v_{a,xz}^k$ is the projected apparent wind speed, A is the wing area, \mathbf{e}_\perp^k and \mathbf{e}_\parallel^k are the unit vectors perpendicular and

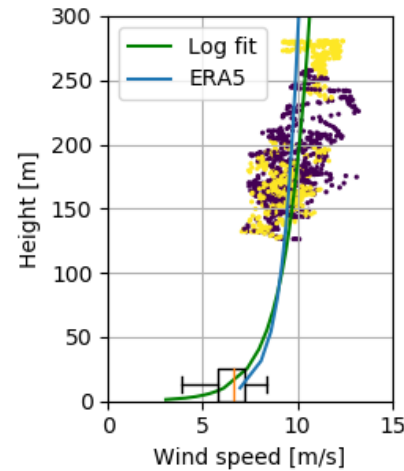


Figure 5. Reconstructed wind speed against the kite height for every data point in the reference pumping cycle. The yellow points are points in either the reel-out or reel-in phase, shown in Fig. 2, for which the kite is not turning. A neutral logarithmic profile with a roughness length of 0.1 m is fitted to the yellow points and depicted together with the ERA5 wind profile at 11:00 AM. The box plot shows the statistics of the wind speed measured at the ground station.

parallel to the apparent wind velocity lying in the kite's symmetry plane, and C_L and C_D are the lift and drag coefficients of the kite. Note that the matrix containing the unit vectors transforms the lift and drag forces to the kite sensor reference frame.

Kite		Tether	
Projected area	19.75 m ²	Density	724 kg/m ³
Mass	22.8 kg	Diameter	10 mm
		$C_{D,tether}$	1.1

Table 1. Properties of the airborne components used for the flight test on 8 October 2019.

The upper-right panel of Fig. 4 shows that the lift and drag coefficients follow a cyclic pattern synchronous to the figure-of-eight manoeuvres during the reel-out phase of the reference cycle. Their mean values during reel-out are 0.71 and 0.14, respectively. A substantial drop in the lift coefficient and increase in the drag coefficient is observed during the left turns. For the first left turn the drop results from an increase in air speed, whereas for the second and third left turns a decrease in air speed is observed. The drop in lift coefficient of the second and third left turns is caused by the relatively low aerodynamic force. During the reel-in phase, the lift coefficient is gradually decreasing: roughly going from 0.45 to 0.33. The mean values of the lift and drag coefficients during reel-in are 0.39 and 0.07, respectively.

4.2. Validation of the system model

The system model that is initially developed by Schmehl [9] is adapted to include the lumping of the tether forces to the kite as proposed by Van der Vlugt [10]. The state of each data point is calculated separately and again assumed to be steady. The system model calculates the apparent wind velocity and infers the attitude of the kite from this velocity together with its position, whereas the kite model infers these properties from measurements. We neglect the vertical wind speed component in the calculation and use the reconstructed horizontal wind speed from Sect. 3.2 as input. Furthermore, we set the values of the aerodynamic coefficients of the kite to those identified in the previous section and the value of the tether force at the ground station with the measured value. The apparent wind velocity is computed using an iterative procedure. Subsequently, the kite velocity follows from subtracting the apparent wind velocity from the wind velocity. The accuracy of the model is assessed by comparing the calculated and measured kite velocity separately for each state.

The measured kite velocity of Eq. 1 is re-expressed in the sphere reference frame, denoted by superscript s_χ , with the x_{s_χ}, y_{s_χ} -plane tangential to the surface of a sphere with its center at the ground station, the z_{s_χ} -axis pointing outwards, and the x_{s_χ} -axis aligned with the tangential projection of the kite velocity. The orientation of the sphere reference frame directly follows from the kite position and velocity. Because the measured values of these properties are used as input for the validation, the measurements and simulations results are expressed in the same reference frame and can be directly compared. Per definition, the y_{s_χ} -component of the kite velocity is zero.

The upper-left panel of Fig. 6 shows that the computed tangential kite speed $v_{k,\tau}$ agrees well with the measurements. The most pronounced bias is roughly 2 m/s at the start of the reel-in phase. The calculated apparent wind velocity strongly depends on the input lift-to-drag ratio. Since the previously identified lift-to-drag ratio is used, the calculated and measured apparent wind velocities are similar. The calculated kite velocity compensates for disregarding the vertical wind speed. The in reality occurring vertical wind speed is attributed to the calculated kite velocity, which causes relatively large discrepancies between the calculated and measured tangential kite speed during the reel-in phase, when the kite speed is relatively low.

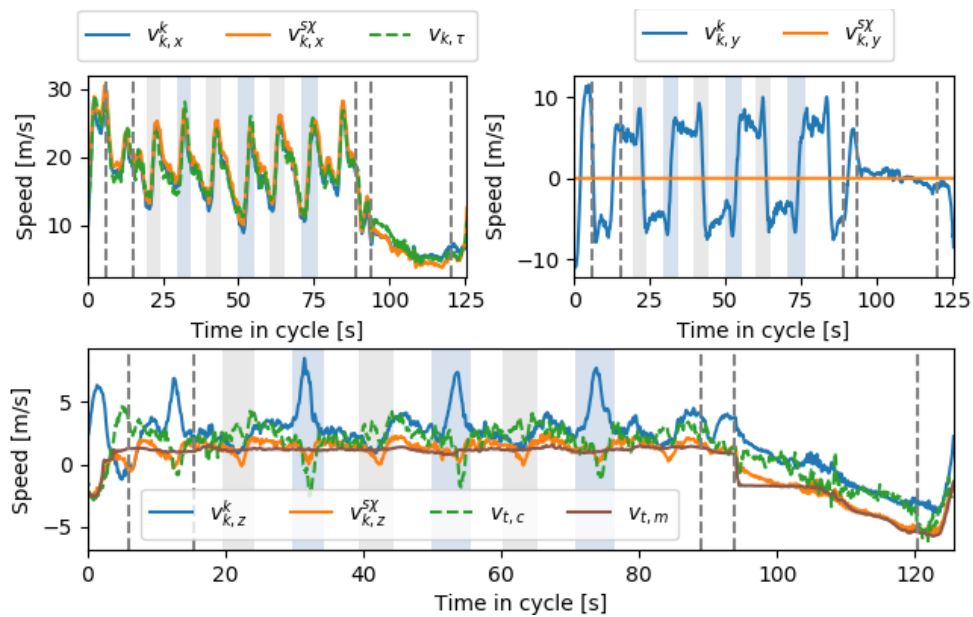


Figure 6. The measured and computed kite velocity components and reeling speed. The computed values are depicted using a dashed line. The measured kite velocity components expressed in both the kite sensor and sphere reference frame are plotted. Although the data points of simulated properties are connected, they are evaluated separately and are not interrelated.

In the lower panel of Fig. 6, the large difference between $v_{k,z}^k$ and $v_{k,z}^{SX}$ for the left turns indicate a relatively large misalignment of the two reference frames. This results from a rolling and pitching motion of the kite that is observed for the left turns, but not for the right turns.

The tether in the system model is assumed to be an infinitely stiff rod. As a result, the modelled reeling speed at the ground and radial kite speed are the same. In reality, this assumption only seems to be valid for the very start of the pumping cycle and the second half of the reel-in phase, where the line for the measured reeling speed $v_{t,m}$ roughly lies on top of that for the measured radial kite speed $v_{k,z}^{SX}$. In between, the two properties are substantially different due to the tether dynamics. This also explains why the agreement between the calculated reeling speed $v_{t,c}$ and the measured reeling speed $v_{t,m}$ is poor. The discrepancy is largest during left turns (blue shade), where the computed reeling speed even becomes negative despite of the system being in the reel-out phase.

Although $v_{k,z}^{SX}$ and $v_{t,c}$ show similar trends, their values differ substantially. The error due to disregarding the vertical wind speed contributes substantially to the mismatch, which is most apparent during the reel-in phase. Again, disregarding the tether dynamics explains for a large part the mismatch during the reel-out phase. Although the computation includes a simple tether sag model, it does not resolve the straightening and slacking motion of the tether. Therefore, the direction in which the tether force is acting varies much more in reality than in the calculations.

5. Quasi-steady model simulations

So far we have only evaluated instantaneous states along the reference pumping cycle. Next, we will apply the reconstructed horizontal wind speeds to perform simulations using the QSM proposed by Van der Vlugt [10]. The kite's motion is approximated as a transition through a series of steady states. The model uses an idealised flight path of the kite, consisting of three phases: the reel-in, transition, and reel-out phase. The cross-wind manoeuvres of the kite are

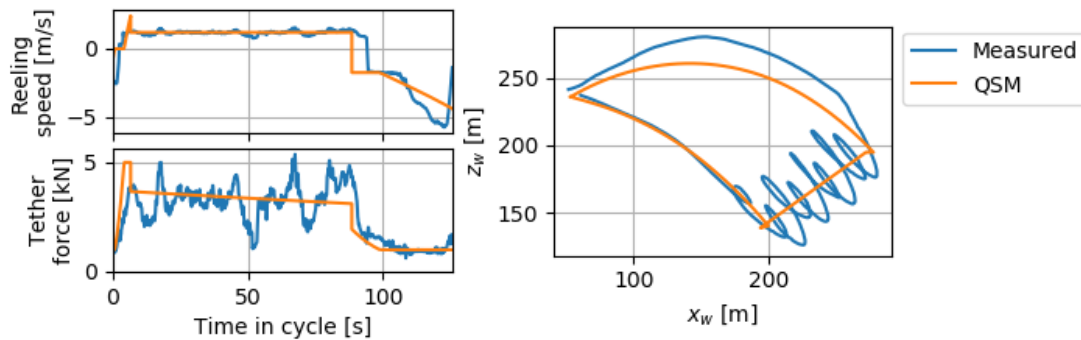


Figure 7. Time series of the controlled properties (left) and side-view of the trajectory (right) for the reference pumping cycle. The equivalent QSM simulation results are plotted alongside flight data.

not resolved and the average performance in the reel-out phase is approximated using a constant elevation, azimuth, and course angle.

The control strategy used for the QSM mimics that of a real flight. In the reel-out phase, a constant reeling speed is imposed, just as for the first part of the reel-in phase. When the lower force limit is reached, the control strategy is switched to a constant tether force control assuring that the tether force does not drop below this lower limit. The measured values of the controlled properties in the reference pumping cycle are plotted with blue lines in the left panels of Fig. 7.

Equivalent QSM simulations are performed for each pumping cycle in the flight data. The wind is modelled as an uniform wind field with its wind speed being set for each phase of each cycle, for which we use the mean reconstructed horizontal wind speed at the kite during the respective phase from Sect. 3.2. Also, the reeling speed setpoint value and tether length properties of the reel-out phase are identified for each cycle from the flight data and used as input for the QSM simulation of that cycle.

Table 2 lists the property values used as input for the equivalent QSM simulation for the reference pumping cycle. The same aerodynamic coefficients are used for simulating the remaining cycles. The mean values of the reference reel-out and reel-in phases, from Sect. 4.1, are used for the powered and de-powered lift coefficients, respectively. The values for the drag coefficients are chosen such that the simulated and measured reel-out tether forces and minimum downwind positions are in good agreement for the reference pumping cycle simulation. The tuned values for the powered and de-powered drag coefficients (0.18 & 0.12) are high compared to the mean values of the reference cycle (0.14 & 0.07). The resulting time series of the controlled properties and side-view of the cycle trajectory are plotted alongside those derived from the flight data in Fig. 7. The tuning of the drag coefficients is equivalent to multiplying them by a fudge factor and thereby turning the QSM into a grey-box model. To obtain an accurate white-box model, some modelling choices in the QSM should be reassessed, e.g., not resolving the cross-wind manoeuvres.

Figure 8 shows the input wind speeds, and the output duration and mean power for each QSM simulation of the pumping cycle, together with the corresponding values derived from flight data. The mean values of the calculated duration and mean power over all cycles are listed in Table 3. The small negative mean error (-1.7%) for the cycle duration indicates that the QSM slightly underpredicts this property. The error of the reel-out and reel-in duration have much larger magnitudes. Because these errors are opposite in sign, they cancel each other out on cycle level. The discrepancies on phase level can partially be explained by different phase definitions used in the QSM and flight data. Note that the mean value of the calculated mean cycle power

	Reel-out	Reel-in		Reel-out	Reel-in
$C_{L,ref}$	0.71	0.39	Setpoint reeling speed	1.19 m/s	-1.75 m/s
$C_{D,tuned}$	0.18	0.12	Tether force		
Elevation	35°		- min.	1 kN	
Azimuth	11.5°	0°	- max.	5 kN	
Course	93°	180°	Tether length		
			- min.	242 m	
			- max.	340 m	

Table 2. Property values used as input for the equivalent QSM simulation of the reference pumping cycle.

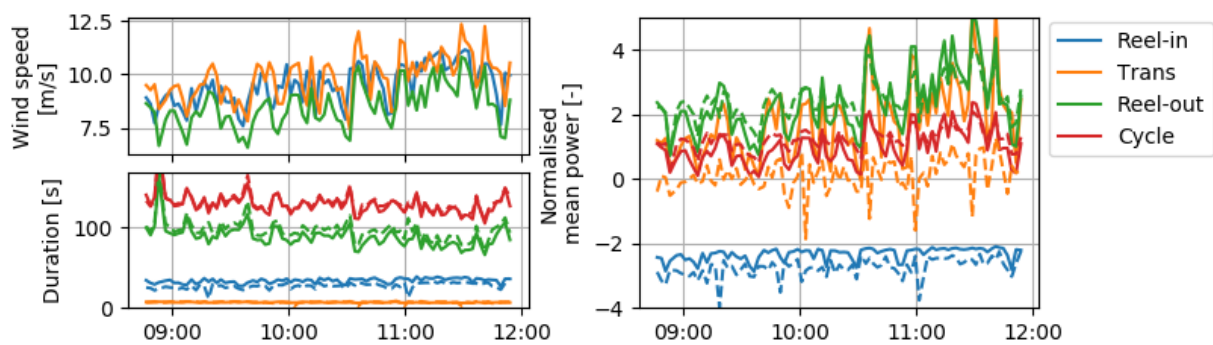


Figure 8. The input and output values of the equivalent QSM simulations of the 87 pumping cycles. The mean reconstructed horizontal wind speeds of the phases that set the respective modelled wind fields for each simulation (upper-left). The duration (lower-left) and normalised mean power (right) of the cycles and their respective phases (reel-out, reel-in, and transition) that result from the simulations (solid lines), together with flight data (dashed lines).

is used for normalising the power ratings. The substantial negative mean error (-26.4%) for the calculated mean cycle power indicates that the QSM underpredicts the energy output. The mean cycle power strongly depends on the duty cycle. The contribution of the duty cycle error to the mean cycle power error yields a high value relative to the mean power errors of the phases. The high mean power error of the transition phase can be explained by discrepancies between the simulation and reality. In the QSM, the kite is allowed to reel out during the transition phase, yielding a positive power output of the system. However, in reality the power output is virtually zero during the transition phase.

		Cycle	Reel-out	Reel-in	Transition
Duration	Calculated [s]	128.8	88.5	33.8	6.5
	Error [s]	-2.2	-8.4	6.5	-0.1
	Error [%]	-1.7	-9.5	19.2	-1.6
Mean power	Calculated & normalised [-]	1.00	2.40	-2.33	1.84
	Error [kW]	-0.35	-0.14	0.57	2.26
	Error [%]	-26.4	-4.3	-18.6	93.8

Table 3. Mean values of the performance indicators over all 87 cycles from the QSM simulations and their mean errors relative to the flight data.

6. Conclusions

The comprehensive dataset of the flight test on 8 October 2019 with the development platform of Kitepower B.V. includes high-quality air flow and kite position and attitude measurements of 87 pumping cycles flown in roughly three hours. The measurements are used to reconstruct the wind conditions at the kite. As the kite sweeps roughly a 150 m height interval in a pumping cycle, also information about the wind profile is acquired. Although an increase in wind speed with height is observed for most cycles, the wind profiles show too much variation to identify a generally applicable wind profile relationship.

The lift and drag coefficients are identified by assuming a steady state of the kite. The approximated force balance acting on the kite yields the aerodynamic force, which is mostly counterbalancing the tether traction force. The aerodynamic coefficients can be inferred from the aerodynamic force. A substantial decrease and increase in the lift and drag coefficients, respectively, is observed during the left turns, which coincides with an unusual rolling and pitching motion of the kite. The mean values of the aerodynamic coefficients are determined for the powered and de-powered kite in the reference cycle. The reference powered lift and drag coefficients are 0.71 and 0.14, respectively, and the reference de-powered lift and drag coefficients are 0.39 and 0.07, respectively.

The reconstructed wind speeds and identified aerodynamic coefficients are used for validating the kite velocity predictions of a steady state system model. The in reality occurring vertical wind speeds are attributed to the kite velocity, which cause large errors in kite velocity during the reel-in phase, when the kite speed is relatively low. The assumption of an infinitely stiff tether is only valid for the transition phase and the second half of the reel-in phase.

The accuracy of the quasi-steady model (QSM) is assessed using steady uniform wind profiles derived from the reconstructed wind speeds. The drag coefficients for the powered and de-powered kite are tuned such that the simulated and measured reel-out tether forces and minimum downwind positions are in good agreement for the reference pumping cycle. The estimated cycle duration is highly accurate with an error of -1.7%. The estimated mean cycle power is less accurate and has an error of -26.4%. The need for tuning the drag coefficient indicates that some modelling choices in the QSM should be reassessed to obtain an accurate white-box model.

Acknowledgements

The authors are grateful to Kitepower B.V. (<http://kitepower.nl>) for sharing their flight data and simulation expertise and in particular to Joep Breurer for giving helpful feedback in our meetings. Also we would like to thank Arthur Roullier for helping implementing the lift and drag coefficients identification procedure. The authors have received financial support by the project REACH (H2020-FTIPilot-691173), funded by the European Union's Horizon 2020 research and innovation programme under grant agreement No. 691173.

References

- [1] Copernicus Climate Change Service (C3S). ERA5: Fifth generation of ECMWF atmospheric reanalyses of the global climate. Copernicus Climate Change Service Climate Data Store (CDS), 2017.
- [2] J. de Schutter et al. Awebox: Python toolbox for modelling and optimal control of multiple-kite systems for airborne wind energy. <https://github.com/awebox/awebox>, 2019.
- [3] S. Gros and M. Diehl. Modeling of airborne wind energy systems in natural coordinates. In U. Ahrens, M. Diehl, and R. Schmehl, editors, *Airborne Wind Energy*, pages 181–203. Springer, Berlin Heidelberg, 2013.
- [4] E.C. Malz, F. Hedenus, L. Göransson, V. Verendel, and S. Gros. Drag-mode airborne wind energy vs. wind turbines: An analysis of power production, variability and geography. *Energy*, 193:116765, 2020.
- [5] E.C. Malz, J. Koenemann, S. Sieberling, and S. Gros. A reference model for airborne wind energy systems for optimization and control. *Renewable Energy*, 140:1004 – 1011, 2019.
- [6] J. Oehler and R. Schmehl. Aerodynamic characterization of a soft kite by in situ flow measurement. *Wind Energy Science*, 4(1):1–21, 2019.

- [7] M. Ranneberg, D. Wölfe, A. Bormann, P. Rohde, F. Breipohl, and I. Bastigkeit. Fast power curve and yield estimation of pumping airborne wind energy systems. In R. Schmehl, editor, *Airborne Wind Energy: Advances in Technology Development and Research*, pages 623–641. Springer Nature, Singapore, 2018.
- [8] M. Schelbergen, P.C. Kalverla, R. Schmehl, and S.J. Watson. Clustering wind profile shapes to estimate airborne wind energy production. *Wind Energy Science Discussions*, 2020.
- [9] R. Schmehl, M. Noom, and R. van der Vlugt. *Traction Power Generation with Tethered Wings*, pages 23–45. Springer Berlin Heidelberg, Berlin, Heidelberg, 2013.
- [10] R. van der Vlugt, A. Bley, M. Noom, and R. Schmehl. Quasi-steady model of a pumping kite power system. *Renewable Energy*, 131:83–99, 2019.